Unusual valence state in the antiperovskites Sr_3SnO and Sr_3PbO revealed by x-ray photoelectron spectroscopy

D. Huang,[1,*] H. Nakamura,[1,†] K. Küster,[1] A. Yaresko,[1] D. Samal,[2,3] N. B. M. Schröter,[4] V. N. Strocov,[4] U. Starke,[1] and H. Takagi[1,5,6]

[1]*Max Planck Institute for Solid State Research, 70569 Stuttgart, Germany*
[2]*Institute of Physics, Bhubaneswar 751005, India*
[3]*Homi Bhabha National Institute, Mumbai 400085, India*
[4]*Swiss Light Source, Paul Scherrer Institute, CH-5232 Villigen PSI, Switzerland*
[5]*Institute for Functional Matter and Quantum Technologies, University of Stuttgart, 70569 Stuttgart, Germany*
[6]*Department of Physics, University of Tokyo, 113-0033 Tokyo, Japan*

(Received 25 September 2019; published 12 December 2019)

The class of antiperovskite compounds A_3BO (A = Ca, Sr, Ba; B = Sn, Pb) has attracted interest as a candidate three-dimensional Dirac system with topological surface states protected by crystal symmetry. A key factor underlying the rich electronic structure of A_3BO is the unusual valence state of B, i.e., a formal oxidation state of -4. Practically, it is not obvious whether anionic B can be stabilized in thin films, due to its unusual chemistry, as well as the polar surface of A_3BO, which may render the growth-front surface unstable. We report x-ray photoelectron spectroscopy measurements of single-crystalline films of Sr_3SnO and Sr_3PbO grown by molecular beam epitaxy. We observe shifts in the core-level binding energies that originate from anionic Sn and Pb, consistent with density functional theory calculations. Near the surface, we observe additional signatures of neutral or cationic Sn and Pb, which may point to an electronic or atomic reconstruction with possible impact on putative topological surface states.

DOI: 10.1103/PhysRevMaterials.3.124203

I. INTRODUCTION

Complex oxides have long provided a rich platform to explore exotic electronic phases that emerge from the interplay of charge, spin, and orbital degrees of freedom [1]. In recent years, efforts to engineer Dirac, Weyl, and other topological semimetallic phases in these compounds have intensified [2]. The effects of strong electronic correlations [3], magnetism [4], and interface reconstructions [5] in complex oxides are expected to enrich the topological phases that can be realized. Such investigations are facilitated by the ability to synthesize these compounds in thin-film heterostructures.

A pertinent example is the class of antiperovskites (or inverse perovskites) with chemical formula A_3BO, where A is an alkaline earth metal (Ca, Sr, or Ba) and B is Sn or Pb. These compounds crystallize into the archetypal perovskite structure but with the usual positions of the cations and anions exchanged [Fig. 1(a)]. These antiperovskites have been predicted to host a unique set of electronic properties. According to rigorous classification, several members of this family are topological crystalline insulators [6] with type-I and type-II Dirac surface states [7]. However, the actual band gap, which lies along the Γ-X line at six equivalent points in the Brillouin zone (BZ), is only a few tens of millielectronvolts, such that in the vicinity of these points, there is a quasilinear three-dimensional (3D) Dirac dispersion [8–10]. Experimentally, angle-resolved photoemission spectroscopy [11], magnetotransport [12,13], and nuclear magnetic resonance [14] measurements have probed the possible 3D Dirac nature of the electrons in these compounds. Experiments have also revealed signatures of ferromagnetism arising from oxygen vacancies [15,16], high thermoelectric performance [17], superconductivity arising from Sr vacancies [18,19], and weak antilocalization due to spin-orbital entanglement [20].

The rich electronic properties of the antiperovskites take as their fundamental origin the unusual valence state of B (= Sn, Pb). In the ionic limit, the constituent elements of A_3BO would exist in the following oxidation states: A^{2+}, B^{4-}, and O^{2-}. We note that Bader analysis reveals that the effective charge of B lies closer to -2 (see Sec. IV). Nevertheless, such a highly anionic state of B implies that a large fraction of its outermost p orbitals are occupied. This configuration produces an unusual situation in A_3BO, wherein the valence bands near the Fermi energy are dominated by B p-orbitals, and the conduction bands near the Fermi energy are dominated by A d-orbitals [Figs. 1(b) and 1(c); refer to Sec. II for details of the band structure calculations]. Around Γ, there is a moderate inversion between the B p-bands and A d-bands. When interorbital hybridization and spin-orbit coupling are taken into account, the six equivalent band crossings at the Fermi energy are only slightly gapped, resulting in the approximate 3D Dirac semimetallic phase [8–10], as well as the topological crystalline insulating phase in some cases [6].

*d.huang@fkf.mpg.de
†hnakamur@uark.edu; Present address: Department of Physics, University of Arkansas, Fayetteville, Arkansas 72701, USA.

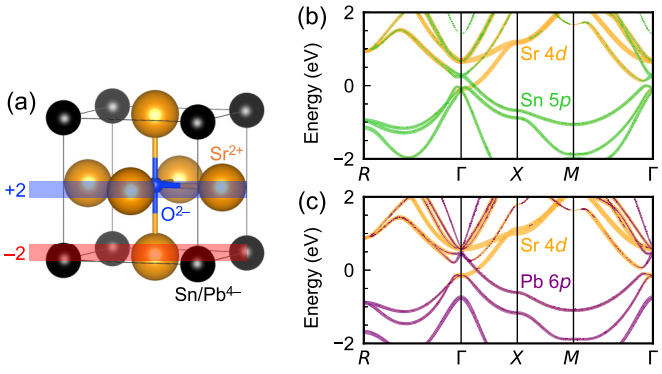

FIG. 1. (a) Crystal structure of the antiperovskite $Sr_3(Sn, Pb)O$. The horizontal bars (red and blue) illustrate polar (001) planes. (b, c) Band structure plots of Sr_3SnO and Sr_3PbO. The thickness of the orange (green/purple) line denotes the weight of the projection of the given state onto the Sr 4*d* (Sn 5*p*/Pb 6*p*) orbitals.

It is natural to ask whether anionic Sn or Pb can be actually stabilized in a thin film. Not only do these anionic states represent unusual chemistry, resulting in extreme air sensitivity, but the antiperovskites may also be prone to surface reconstruction. As illustrated in Fig. 1(a), the (001) planes alternate between an overall oxidation state of +2 and −2, leading to a polar catastrophe at a surface [21]. To alleviate a divergence in the electrostatic potential, it is possible that Sr vacancies form at the surface (analogous to O vacancies in oxide perovskites) and/or Sn and Pb shift to a more stable valence state (neutral or cationic) via electronic reconstruction. If so, this has profound implications on surface states [7], similar to the case of the Kondo insulator SmB_6, whose polar surface has complicated the elucidation of its topological properties [22].

Previous measurements of bulk $Sr_{3-x}SnO$ crystals uncovered signatures of anionic Sn [19]. Using ^{119}Sn Mössbauer spectroscopy, Oudah *et al.* observed an isomer shift of the main peak by +1.88 mm/s, matching that of Mg_2Sn, another compound in which Sn is formally −4. The situation in thin films, however, is less clear. Minohara *et al.* performed x-ray photoelectron spectroscopy (XPS) measurements of Ca_3SnO films under ultrahigh vacuum (UHV) [23]. The reported Sn $3d_{5/2}$ spectrum showed a surface component corresponding to Sn^{4+} or Sn^{2+}, as well as a bulk component which they attributed to the antiperovskite phase. However, the bulk component had a binding energy of 484.8 eV, lying within the range expected for neutral Sn: 484.3-485.2 eV [24]. Further investigation is needed to clarify the anionic state of Sn in thin films.

Here, we performed XPS measurements of Sr_3SnO and Sr_3PbO films grown by molecular beam epitaxy (MBE) and kept in UHV conditions. In the bulk, we observe peaks in the Sn 3*d* and Pb 4*f* core levels that lie at lower binding energies than those of cationic or neutral Sn and Pb. Density functional theory (DFT) calculations confirm that these shifts match predictions for anionic Sn (Pb) in Sr_3SnO (Sr_3PbO). At the surface, we find signatures of cationic and neutral Sn and Pb, consistent with the scenario of an atomic or electronic reconstruction at the surface.

II. METHODS

Films of Sr_3SnO and Sr_3PbO with thickness ∼100 nm were grown in an Eiko MBE chamber with base pressure in the low 10^{-9} mbar range. The films were deposited on (001)-cut substrates of yttria-stabilized zirconia (YSZ), which were precoated at two opposite edges with Au or Nb for electrical grounding in XPS measurements. Elemental sources of Sr (99.9% purity from vendor, further refined in house by sublimation), Sn (99.999% purity), and Pb (99.999% purity) were thermally sublimated from effusion cells. A mixture of 2% O_2 in Ar gas was supplied through a leak valve (pressure range 10^{-6}–10^{-5} mbar). Since the samples reported in this work were grown at different times spanning a two-year period, different growth parameters were used in the course of optimizing film quality (example parameters can be found in Refs. [20,25]). We will not focus on these systematic differences but instead on the ubiquitous observation of an antiperovskite phase via XPS.

Following growth, the films were examined *in situ* using reflection high-energy electron diffraction (RHEED) and then transferred in vacuum suitcases (Ferrovac GmbH; pressure range: low 10^{-10} mbar) for XPS measurements. We note that other films grown with identical conditions to these were capped with Au or Apiezon-N grease in an Ar glove box then characterized by x-ray diffraction (XRD) and/or transport [20,25].

XPS data were acquired at the Max Planck Institute for Solid State Research (MPI-FKF) in a system equipped with a commercial Kratos AXIS Ultra spectrometer and a monochromatized Al $K\alpha$ source (photon energy 1486.6 eV). The base pressure was in the low 10^{-10} mbar range. An analyzer pass energy of 20 eV was used to collected detailed spectra. In addition to the antiperovskite films, we measured reference spectra from a Sn film (grown using MBE, transported in a vacuum suitcase) and a Pb foil (cleaned *in situ* using Ar sputtering). The Sn film [Fig. 3(b)] showed charging due to poor electrical grounding; in this instance, we used the Fermi edge to recalibrate the binding energy. We also performed low-energy electron diffraction (LEED) on our films in an adjoining chamber equipped with a commercial SPECS Er-LEED 150 system.

XPS spectra were analyzed using the CASAXPS software. To fit the various peaks, we used multiple Gaussian-Lorentzian mixture functions on top of a Shirley background. To constrain our fitting parameters, we fixed the doublet spacing energy of Sn 3*d*, Sr 3*d*, and Pb 4*f* to their literature values of 8.41, 1.79, and 4.86 eV, respectively [26]. We also constrained the area ratio of the doublets to 2:3 for *d* core levels and 3:4 for *f* core levels.

We also collected XPS data at grazing emission which are more sensitive to the surface elemental composition. This allowed us to disentangle surface and bulk contributions in the XPS spectra. Similarly, for films measured at the ADRESS beamline of the Swiss Light Source (SLS) [27,28], we were able to control the surface sensitivity by tuning the photon energy [29].

We performed DFT calculations using the Vienna *ab initio* simulation package VASP [30,31], which implements the projector augmented-wave (PAW) method [32,33]. The following

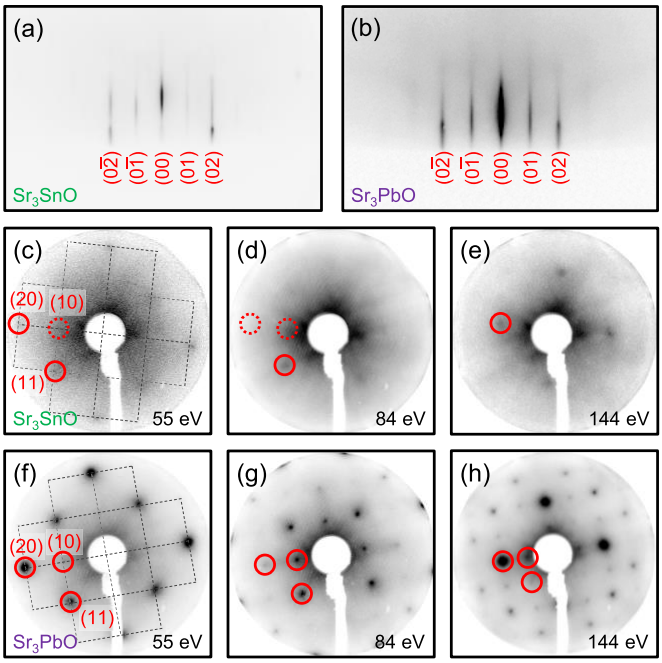

FIG. 2. (a, b) RHEED images of Sr_3SnO (sample SS91) and Sr_3PbO (sample AP389) taken along the [100] direction. Electron energy: 15 keV. (c)–(e) LEED images of Sr_3SnO (sample SS60) acquired at 55, 84, and 144 eV. (f)–(h) LEED images of Sr_3PbO (sample AP149) acquired at the same energies.

electrons were treated as valence: $3s3p4s$ in Ca, $4s4p5s$ in Sr, $5s5p6s$ in Ba, $5s4d5p$ in Sn, $6s5d6p$ in Pb, and $2s2p$ in O. We used the generalized gradient approximation (GGA) as parameterized by Perdew, Burke, and Ernzerhof (PBE) [34]. An energy cutoff of 750 eV was used, along with a BZ sampling as dense as $28 \times 28 \times 28$ for the self-consistent calculation of the charge density. For the band structure calculations shown in Figs. 1(b) and 1(c), spin-orbit coupling

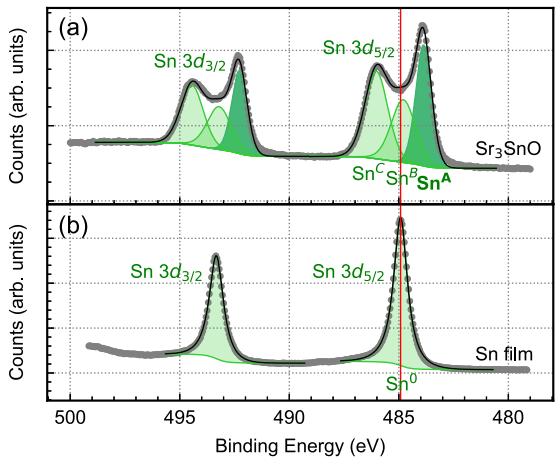

FIG. 3. (a) XPS spectrum of the Sn $3d_{3/2}$ and $3d_{5/2}$ doublet of Sr_3SnO (sample SS91) acquired at MPI-FKF with photon energy 1486.6 eV. The gray circles are the measured data, the black line is the overall fit, and the green shaded areas are the individual peaks that constitute the fit. (b) A reference spectrum for a thin film of metallic Sn is shown for comparison with (a).

TABLE I. Binding energies of peaks extracted from fits to the Sn $3d_{5/2}$ level of Sr_3SnO. As described in the main text, Sn^A is assigned to the bulk antiperovskite phase, whereas Sn^B and Sn^C are ascribed to a surface layer present in the films. The binding energy of Sn^0, extracted from a reference Sn film, is also reported.

	Sn^A [eV]	Sn^B [eV]	Sn^C [eV]
SS60 [Fig. 4(b)]	483.82	484.72	486.02
SS91 [Fig. 3(a)]	483.87	484.79	486.03
	Sn^0 [eV]		
Sn film [Fig. 3(b)]	484.92		

was included in an additional non-self-consistent cycle. We also performed Bader charge analysis. Estimates of core-level shifts, which we performed using both VASP and PY LMTO, will be discussed in Sec. IV. Atomic structures were visualized using VESTA [35].

III. RESULTS AND DISCUSSION

A. RHEED and LEED

Figures 2(a) and 2(b) show RHEED images acquired along the [100] direction of Sr_3SnO and Sr_3PbO, respectively. We note that the underlying YSZ substrate and a thin SrO buffer layer deposited prior to the antiperovskite are also cubic with similar lattice constants. However, they are forbidden by their crystal structure from exhibiting $(0l)$ streaks with odd integer l. Hence, the appearance of the (01) streak establishes the existence of the target antiperovskite phase.

Figures 2(c)–2(e) and 2(f)–2(h) show LEED images acquired at different energies for Sr_3SnO and Sr_3PbO, respectively. The square array of the diffraction spots is consistent with the antiperovskite crystal structure. In addition, the complex evolution of the structure factor as a function of electron energy is observed [36]. In general, LEED images of Sr_3PbO exhibit brighter patterns than those of Sr_3SnO, and this is also reflected in the RHEED streaks. As discussed in the following two sections, XPS measurements show that both the Sr_3SnO and Sr_3PbO films have a thin surface layer covering the bulk antiperovskite phase. The brighter RHEED/LEED images in Sr_3PbO may point to a thinner surface layer covering Sr_3PbO or to the stronger scattering strength of Pb compared to Sn.

B. Sr_3SnO XPS

Figure 3(a) presents the Sn $3d$ spectrum of a Sr_3SnO film (SS91). As clearly seen, each of the spin-split levels ($3d_{3/2}$ and $3d_{5/2}$) exhibits two pronounced peaks indicative of multiple Sn valence states. Using the fitting procedure described in Sec. II, we find that actually, a minimum of three Gaussian-Lorentzian mixture functions are required to fit each level. For the Sn $3d_{5/2}$ level, the three peaks are centered at 483.87, 484.79, and 486.03 eV (Table I). We label these peaks Sn^A, Sn^B, and Sn^C, respectively [Fig. 3(a)].

To understand the origin of these peaks, we performed XPS measurements on a control sample, a thin film of Sn deposited on YSZ [Fig. 3(b)]. The Sn $3d_{5/2}$ level shows a sharp peak centered at 484.92 eV, closely matching the literature value for metallic Sn, 485.0 eV [26]; we thus label

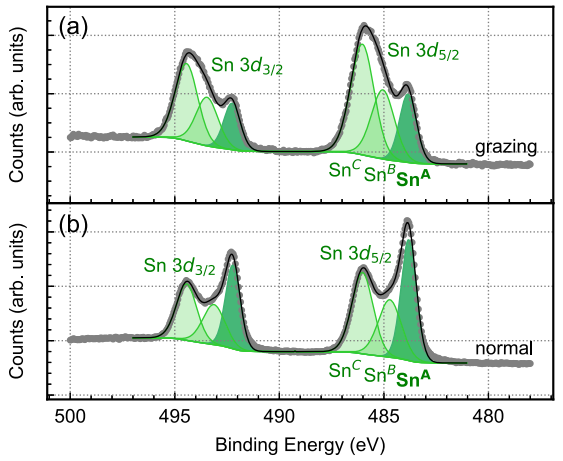

FIG. 4. Angle dependence. Sn 3*d* spectra of sample SS60 taken at (a) grazing (60° off normal) and (b) normal emission. Data were acquired at MPI-FKF with photon energy $h\nu = 1486.6$ eV.

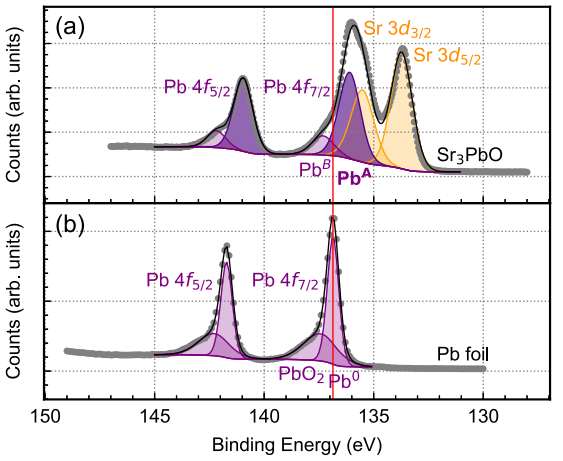

FIG. 5. (a) XPS spectrum of the Sr $3d_{3/2}$ and $3d_{5/2}$ doublet and the Pb $4f_{5/2}$ and $4f_{7/2}$ doublet of Sr_3PbO (sample AP337) acquired at MPI-FKF with photon energy 1486.6 eV. The gray circles are the measured data, the black line is the overall fit, and the orange (purple) shaded areas are the individual Sr (Pb) peaks that constitute the fit. (b) A reference spectrum for a metallic Pb foil is shown for comparison with (a).

this peak Sn^0. Comparing with the spectrum from Sr_3SnO [Fig. 3(a)], we note that Sn^0 overlaps with Sn^B. Sn^C, with higher binding energy, matches literature values for SnO [26], or SnO_2 [37]. Sn^A, with lower binding energy, could be assigned to the antiperovskite phase. Intuitively, Sn states with higher binding energy than Sn^0 (red line in Fig. 3) are cationic (positively charged), such that core electrons are less readily removed, whereas Sn states with lower binding energy than Sn^0 are anionic (negatively charged), such that core electrons are more readily removed. Indeed, XPS measurements of Ni_3Sn_4 electrodes for Li-ion batteries showed that when Sn was lithiated and therefore negatively charged, the $3d_{5/2}$ peak corresponding to Sn^0 shifted to lower binding energies [38].

The dependence of the Sn 3*d* spectra on the emission angle of the electrons is shown in Fig. 4 for another Sr_3SnO film (SS60). The spectrum obtained at grazing emission is more surface sensitive than that at normal emission. We observe that near the surface, Sn^B and Sn^C occupy a greater fraction of the total intensity than Sn^A [Fig. 4(a)]. Deeper into the bulk, however, Sn^A is enhanced relative to Sn^B and Sn^C [Fig. 4(b)]. Thus, the bulk phase of our film is characterized by Sn^A, consistent with anionic Sn in Sr_3SnO. Nevertheless, there is a surface layer in which Sn reverts to its neutral ($Sn^B \sim Sn^0$) and cationic ($Sn^C \sim$ SnO or SnO_2) states, likely originating from the unstable polar (001) surface of Sr_3SnO. Since an electron with kinetic energy on the order of 1 keV has an inelastic mean free path on the order of 1 nm [39], we deduce the surface layer to have thickness less than 1 nm.

C. Sr_3PbO XPS

In essence, the XPS results of Sr_3PbO are similar to the Sr_3SnO results. Figure 5(a) presents the overlapping Sr 3*d* and Pb 4*f* spectra of a Sr_3PbO film (AP337). Two Gaussian-Lorentzian mixture functions were required to fit the Pb 4*f* levels, with peaks $Pb^A = 136.10$ eV and $Pb^B = 137.32$ eV (Table II). To identify these peaks, we again performed XPS measurements on a control sample, a Pb foil cleaned *in situ* by Ar sputtering [Fig. 5(b)]. The Pb $4f_{7/2}$ level shows a pronounced peak centered at 136.86 eV, close to the literature value for metallic Pb, 136.9 eV [26]; we thus label this peak Pb^0. There is also a residual peak at higher binding energies, 137.43 eV, which agrees with literature values for PbO_2 [26]. Comparing with the data from Sr_3PbO [Fig. 5(a)], we observe that Pb^B overlaps with PbO_2, whereas Pb^A is exclusive to the antiperovskite film. Its lower binding energy relative to Pb^0 indicates that it is anionic.

Figure 6 presents the angle dependence of the overlapping Sr 3*d* and Pb 4*f* spectra, along with fits, for sample AP149. At grazing emission, Pb^B dominates the spectrum, but at normal emission, the intensity of Pb^A is enhanced relative to Pb^B. Again, we conclude that the bulk phase of our film is characterized by Pb^A, which we assign to anionic Pb in Sr_3PbO, but in a thin surface layer, Pb reverts to its cationic state ($Pb^B \sim PbO_2$).

At the given photon energy of 1486.6 eV, with normal emission, the XPS signal from the surface layer appears to be less significant in Sr_3PbO [Figs. 5(a) and 6(b)] than in Sr_3SnO [Figs. 3(a) and 4(b)]. This could be attributed to the difference in kinetic energy of the emitted electron: the higher binding energy for the Sn 3*d* core levels relative to the Pb 4*f* core levels may cause the XPS signal for Sr_3PbO to be

TABLE II. Binding energies of peaks extracted from fits to the Pb $4f_{7/2}$ level of Sr_3PbO. As described in the main text, Pb^A is assigned to the bulk antiperovskite phase, whereas Pb^B is ascribed to a surface layer present in the films. The binding energies of Pb^0 and PbO_2, extracted from a reference Pb foil, are also reported.

	Pb^A [eV]	Pb^B [eV]
AP149 [Fig. 6(b)]	136.10	137.42
AP337 [Fig. 5(a)]	136.10	137.32
	Pb^0 [eV]	PbO_2 [eV]
Pb foil [Fig. 5(b)]	136.86	137.43

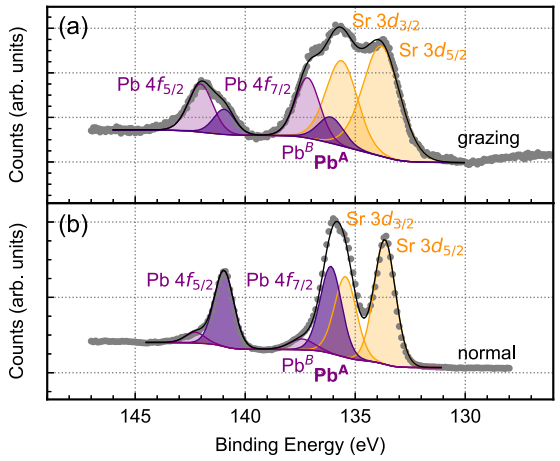

FIG. 6. Angle dependence. Sr $3d$ and Pb $4f$ spectra of sample AP149 taken at (a) grazing (60° off normal) and (b) normal emission. Data were acquired at MPI-FKF with photon energy $h\nu = 1486.6$ eV.

more bulk sensitive. As a result, it is possible that neutral Pb exists in the surface layer of Sr_3PbO, similar to Sr_3SnO, but the signal is too small to detect. Alternatively, the surface layer in Sr_3PbO could simply be thinner. It is possible that anionic Pb is intrinsically more stable and less prone to oxidation than anionic Sn.

IV. DENSITY FUNCTIONAL THEORY

In this section, we use DFT to demonstrate that in the antiperovskite compounds A_3BO, B (= Sn, Pb) does indeed carry a negative effective charge, consistent with the heuristic concept of formal oxidation states. Then we show that the XPS binding energy of the Sn^A (Pb^A) peak in Sr_3SnO (Sr_3PbO) relative to the Sn^0 (Pb^0) peak in metallic Sn (Pb) matches predictions by DFT calculations. This further confirms our assignment of the Sn^A and Pb^A peaks to the bulk antiperovskite phase at a quantitative level.

A. Effective charges

While formal oxidation states are a useful construct when examining chemical bonding or electronic structure, they are not identical to the actual effective charges surrounding each atom. Generally, bonds in a crystal exhibit a greater degree of covalency than is expected in a pure ionic picture. To compute the effective charges, we used Bader's method of partitioning the charge density via zero-flux surfaces [40]. Table III presents effective charges computed for various antiperovskites. The effective charge of B (= Sn, Pb) averages around -2 across the compounds considered. Thus, while the effective charge is clearly lower than the value of -4 expected from formal oxidation states, it is still clear that B is unusually anionic. We note a trend that as the size of A increases from Ca to Sr to Ba, the effective charge of B becomes less negative [10].

B. Core-level shifts

Experimentally, what XPS measures is neither the formal oxidation state nor the effective charge but shifts in the core-level binding energies. We therefore used DFT to quantitatively confirm the shift towards lower binding energies for anionic B relative to metallic B. To calculate the core-level binding energies (E_c), we worked within the initial state approximation, wherein a selected core electron is removed but the remaining electrons are kept frozen [41]. Then E_c is simply given by the Kohn-Sham (KS) eigenvalue of the core electron (ϵ_c), relative to the Fermi energy (ϵ_F):

$$E_c = -(\epsilon_c - \epsilon_F). \quad (1)$$

While final state effects, primarily the screening of the core hole, are neglected, the initial state approximation captures the chemical state of the atom as reflected in its valence charge configuration [42].

In the PAW formalism of VASP, ϵ_c is computed in two steps [41]: First, the core electrons are frozen and the valence charge density is computed via the normal, self-consistent electronic relaxation. Second, the KS eigenvalues for the core electrons are solved inside the PAW spheres while keeping the valence charge density fixed. As a check, we also performed all-electron PBE GGA calculations using the relativistic linear muffin-tin orbital (LMTO) method as implemented in the PY LMTO computer code. Here, spin-orbit coupling was included by solving the Dirac equations inside the atomic spheres. Some details of the implementation can be found in Ref. [43].

The absolute values of E_c as determined from the KS eigenvalues of DFT are typically 20–30 eV lower than the experimental values reported by XPS due to a breakdown of Koopman's theorem [44]. However, DFT does provide meaningful values of ΔE_c, the shift of the core-level binding energy between two systems. In a study, van Setten *et al.* demonstrated that for a set of molecules containing C, O, N, or F, the mean absolute difference between ΔE_c, as calculated from the KS eigenvalues, and the actual core-level shifts, as measured by XPS, was only 0.74 eV [44].

To make a meaningful comparison with our data, we took metallic Sn (α allotrope, diamond structure) and metallic Pb (face-centered cubic) as our references. We calculated $\Delta E_{\mathrm{Sn}\,3d}$ between Sr_3SnO and α-Sn, and $\Delta E_{\mathrm{Pb}\,4f}$ between Sr_3PbO and Pb. Dense BZ sampling and a high energy cutoff, as stated previously, were needed to converge the core-level binding energies within 1 meV. The results are shown in Table IV, computed using the following experimental lattice constants: 5.139 Å for Sr_3SnO, 6.489 Å for α-Sn, 5.151 Å for Sr_3PbO, and 4.950 Å for Pb [45–47]. We note that in the case of $\Delta E_{\mathrm{Sn}\,3d}$, there is a shift by +0.12 eV when the DFT-optimized lattice parameter is used due to a discrepancy of 2.5% between

TABLE III. Effective charges computed by Bader analysis for various antiperovskites A_3BO.

	A = Ca/Sr/Ba	B = Sn/Pb	O
Ca_3SnO	+1.30	−2.38	−1.51
Ca_3PbO	+1.29	−2.35	−1.52
Sr_3SnO	+1.26	−2.30	−1.48
Sr_3PbO	+1.25	−2.26	−1.48
Ba_3SnO	+1.14	−1.98	−1.44
Ba_3PbO	+1.12	−1.93	−1.44

TABLE IV. Comparison between DFT and XPS. The core-level shifts, as predicted by DFT, are given by $\Delta E_{\mathrm{Sn}\,3d} = E_{\mathrm{Sn}\,3d}(\mathrm{Sr_3SnO}) - E_{\mathrm{Sn}\,3d}(\alpha\text{-Sn})$ and $\Delta E_{\mathrm{Pb}\,4f} = E_{\mathrm{Pb}\,4f}(\mathrm{Sr_3PbO}) - E_{\mathrm{Pb}\,4f}(\mathrm{Pb})$. Results from two different codes (VASP and PY LMTO) are shown. The core-level shifts, as measured by XPS, are given by the difference between the Sn^A peak in $\mathrm{Sr_3SnO}$ and the Sn^0 peak in metallic Sn, or between the Pb^A peak in $\mathrm{Sr_3PbO}$ and the Pb^0 peak in metallic Pb.

DFT: $\Delta E_{\mathrm{Sn}\,3d}$ [eV]	DFT: $\Delta E_{\mathrm{Pb}\,4f}$ [eV]
VASP: −0.95	VASP: −0.79
PY LMTO: −1.14	PY LMTO: −0.98
XPS: $\mathrm{Sn}^A - \mathrm{Sn}^0$ [eV]	XPS: $\mathrm{Pb}^A - \mathrm{Pb}^0$ [eV]
SS60: −1.10	AP149: −0.76
SS91: −1.05	AP337: −0.76

the experimental and DFT-optimized lattice constants of α-Sn. We also note that differences in ΔE_c arising from the use of the local density approximation (LDA) instead of GGA are within 0.1 eV.

Shown in Table IV are also the core-level shifts as measured by XPS. For the $\mathrm{Sr_3SnO}$ films, we took the difference between the Sn^A peak, which we ascribed to the bulk antiperovskite phase, and the Sn^0 peak in the reference Sn metal. Similarly, the difference between Pb^A in $\mathrm{Sr_3PbO}$ and Pb^0 in Pb metal was used to derive the shift for $\mathrm{Sr_3PbO}$. The DFT and XPS results for the core-level shifts show a very good agreement. Furthermore, in both theory and experiment, the magnitude of the shift is larger in Sn $3d$ compared to Pb $4f$. Hence, we conclude again with additional confirmation that the Sn^A (Pb^A) peak corresponds to anionic Sn (Pb) in $\mathrm{Sr_3SnO}$ ($\mathrm{Sr_3PbO}$).

V. SUMMARY

In this work, we have investigated the antiperovskites $\mathrm{Sr_3SnO}$ and $\mathrm{Sr_3PbO}$, whose predicted topological crystalline insulating phase and approximate 3D Dirac semimetallic phase hinge upon the stabilization of Sn and Pb in an unusual anionic state (~ -2 according to Bader charge analysis). Our XPS measurements, along with DFT calculations, confirm that anionic Sn and Pb do indeed exist in thin films of $\mathrm{Sr_3SnO}$ and $\mathrm{Sr_3PbO}$. Interestingly, though, we observed signatures of cationic or neutral Sn and Pb distributed at the surface of the films. This suggests that the polar (001) surface of these antiperovskites is susceptible to a reconstruction wherein the valence states of Sn and Pb are altered. Such a modification is likely to have drastic impact on the surface electronic structure. We suggest using scanning tunneling microscopy to elucidate the nature of potential surface reconstruction (electronic or atomic) and its effects on putative topological surface states.

ACKNOWLEDGMENTS

We thank U. Wedig for helpful discussions. We also thank M. Konuma, C. Mühle, K. Pflaum, S. Prill-Diemer, and S. Schmid for technical assistance at MPI-FKF. We acknowledge the Paul Scherrer Institut, Villigen, Switzerland, for provision of synchrotron radiation beam time at the ADRESS beamline of the SLS. D.H. acknowledges support from a Humboldt Research Fellowship for Postdoctoral Researchers. N.B.M.S. acknowledges partial financial support from Microsoft.

[1] M. Imada, A. Fujimori, and Y. Tokura, Metal-insulator transitions, Rev. Mod. Phys. **70**, 1039 (1998).

[2] M. Uchida and M. Kawasaki, Topological properties and functionalities in oxide thin films and interfaces, J. Phys. D **51**, 143001 (2018).

[3] J. Fujioka, R. Yamada, M. Kawamura, S. Sakai, M. Hirayama, R. Arita, T. Okawa, D. Hashizume, M. Hoshino, and Y. Tokura, Strong-correlation induced high-mobility electrons in Dirac semimetal of perovskite oxide, Nat. Commun. **10**, 362 (2019).

[4] X. Wan, A. M. Turner, A. Vishwanath, and S. Y. Savrasov, Topological semimetal and Fermi-arc surface states in the electronic structure of pyrochlore iridates, Phys. Rev. B **83**, 205101 (2011).

[5] H. Y. Hwang, Y. Iwasa, M. Kawasaki, B. Keimer, N. Nagaosa, and Y. Tokura, Emergent phenomena at oxide interfaces, Nat. Mater. **11**, 103 (2012).

[6] T. H. Hsieh, J. Liu, and L. Fu, Topological crystalline insulators and Dirac octets in antiperovskites, Phys. Rev. B **90**, 081112(R) (2014).

[7] C.-K. Chiu, Y.-H. Chan, X. Li, Y. Nohara, and A. P. Schnyder, Type-II Dirac surface states in topological crystalline insulators, Phys. Rev. B **95**, 035151 (2017).

[8] T. Kariyado and M. Ogata, Three-dimensional Dirac electrons at the Fermi energy in cubic inverse perovskites: $\mathrm{Ca_3PbO}$ and its family, J. Phys. Soc. Jpn. **80**, 083704 (2011).

[9] T. Kariyado and M. Ogata, Low-energy effective Hamiltonian and the surface states of $\mathrm{Ca_3PbO}$, J. Phys. Soc. Jpn. **81**, 064701 (2012).

[10] T. Kariyado and M. Ogata, Evolution of band topology by competing band overlap and spin-orbit coupling: Twin Dirac cones in $\mathrm{Ba_3SnO}$ as a prototype, Phys. Rev. Mater. **1**, 061201 (2017).

[11] Y. Obata, R. Yukawa, K. Horiba, H. Kumigashira, Y. Toda, S. Matsuishi, and H. Hosono, ARPES studies of the inverse perovskite $\mathrm{Ca_3PbO}$: Experimental confirmation of a candidate 3D Dirac fermion system, Phys. Rev. B **96**, 155109 (2017).

[12] S. Suetsugu, K. Hayama, A. W. Rost, J. Nuss, C. Mühle, J. Kim, K. Kitagawa, and H. Takagi, Magnetotransport in $\mathrm{Sr_3PbO}$ antiperovskite, Phys. Rev. B **98**, 115203 (2018).

[13] Y. Obata, Y. Kohama, S. Matsuishi, and H. Hosono, Shubnikov–de Haas oscillations in the three-dimensional Dirac fermion system $\mathrm{Ca_3PbO}$, Phys. Rev. B **99**, 115133 (2019).

[14] S. Kitagawa, K. Ishida, M. Oudah, J. N. Hausmann, A. Ikeda, S. Yonezawa, and Y. Maeno, Normal-state properties of the

antiperovskite oxide $Sr_{3-x}SnO$ revealed by ^{119}Sn-NMR, Phys. Rev. B **98**, 100503(R) (2018).

[15] Y. F. Lee, F. Wu, R. Kumar, F. Hunte, J. Schwartz, and J. Narayan, Epitaxial integration of dilute magnetic semiconductor Sr_3SnO with Si (001), Appl. Phys. Lett. **103**, 112101 (2013).

[16] Y. F. Lee, F. Wu, J. Narayan, and J. Schwartz, Oxygen vacancy enhanced room-temperature ferromagnetism in Sr_3SnO/c-YSZ/Si (001) heterostructures, MRS Commun. **4**, 7 (2014).

[17] Y. Okamoto, A. Sakamaki, and K. Takenaka, Thermoelectric properties of antiperovskite calcium oxides Ca_3PbO and Ca_3SnO, J. Appl. Phys. **119**, 205106 (2016).

[18] M. Oudah, A. Ikeda, J. N. Hausmann, S. Yonezawa, T. Fukumoto, S. Kobayashi, M. Sato, and Y. Maeno, Superconductivity in the antiperovskite Dirac-metal oxide $Sr_{3x}SnO$, Nat. Commun. **7**, 13617 (2016).

[19] M. Oudah, J. N. Hausmann, S. Kitao, A. Ikeda, S. Yonezawa, M. Seto, and Y. Maeno, Evolution of superconductivity with Sr-deficiency in antiperovskite oxide $Sr_{3x}SnO$, Sci. Rep. **9**, 1831 (2019).

[20] H. Nakamura, J. Merz, E. Khalaf, P. Ostrovsky, A. Yaresko, D. Samal, and H. Takagi, Robust weak antilocalization due to spin-orbital entanglement in Dirac material Sr_3SnO, arXiv:1806.08712.

[21] A. Ohtomo and H. Hwang, A high-mobility electron gas at the $LaAlO_3/SrTiO_3$ heterointerface, Nat. (London) **427**, 423 (2004).

[22] Z.-H. Zhu, A. Nicolaou, G. Levy, N. P. Butch, P. Syers, X. F. Wang, J. Paglione, G. A. Sawatzky, I. S. Elfimov, and A. Damascelli, Polarity-Driven Surface Metallicity in SmB_6, Phys. Rev. Lett. **111**, 216402 (2013).

[23] M. Minohara, R. Yukawa, M. Kitamura, R. Kumai, Y. Murakami, and H. Kumigashira, Growth of antiperovskite oxide Ca_3SnO films by pulsed laser deposition, J. Cryst. Growth **500**, 33 (2018).

[24] NIST X-ray Photoelectron Spectroscopy Database, NIST Standard Reference Database Number 20, Online, available at https://srdata.nist.gov/xps/, National Institute of Standards and Technology, Gaithersburg MD, 20899, 2000.

[25] D. Samal, H. Nakamura, and H. Takagi, Molecular beam epitaxy of three-dimensional Dirac material Sr_3PbO, APL Mater. **4**, 076101 (2016).

[26] J. Moulder and J. Chastain, *Handbook of X-ray Photoelectron Spectroscopy: A Reference Book of Standard Spectra for Identification and Interpretation of XPS Data* (Physical Electronics Division, Perkin-Elmer Corporation, 1992).

[27] V. N. Strocov, T. Schmitt, U. Flechsig, T. Schmidt, A. Imhof, Q. Chen, J. Raabe, R. Betemps, D. Zimoch, J. Krempasky, X. Wang, M. Grioni, A. Piazzalunga, and L. Patthey, High-resolution soft X-ray beamline ADRESS at the Swiss Light Source for resonant inelastic X-ray scattering and angle-resolved photoelectron spectroscopies, J. Synchrotron Radiat. **17**, 631 (2010).

[28] V. N. Strocov, X. Wang, M. Shi, M. Kobayashi, J. Krempasky, C. Hess, T. Schmitt, and L. Patthey, Soft-X-ray ARPES facility at the ADRESS beamline of the SLS: Concepts, technical realisation and scientific applications, J. Synchrotron Radiat. **21**, 32 (2014).

[29] See Supplemental Material at http://link.aps.org/supplemental/10.1103/PhysRevMaterials.3.124203 for additional XPS spectra, photon energy dependence, position dependence, and fit parameters.

[30] G. Kresse and J. Furthmüller, Efficiency of *ab-initio* total energy calculations for metals and semiconductors using a plane-wave basis set, Comput. Mater. Sci. **6**, 15 (1996).

[31] G. Kresse and J. Furthmüller, Efficient iterative schemes for *ab-initio* total-energy calculations using a plane-wave basis set, Phys. Rev. B **54**, 11169 (1996).

[32] P. E. Blöchl, Projector augmented-wave method, Phys. Rev. B **50**, 17953 (1994).

[33] G. Kresse and D. Joubert, From ultrasoft pseudopotentials to the projector augmented-wave method, Phys. Rev. B **59**, 1758 (1999).

[34] J. P. Perdew, K. Burke, and M. Ernzerhof, Generalized Gradient Approximation Made Simple, Phys. Rev. Lett. **77**, 3865 (1996).

[35] K. Momma and F. Izumi, *VESTA3* for three-dimensional visualization of crystal, volumetric and morphology data, J. Appl. Crystallogr. **44**, 1272 (2011).

[36] M. A. Van Hove, W. H. Weinberg, and C.-M. Chan, *Low-Energy Electron Diffraction: Experiment, Theory and Surface Structure Determination* (Springer, Berlin, 1986).

[37] J.-M. Themlin, M. Chtaïb, L. Henrard, P. Lambin, J. Darville, and J.-M. Gilles, Characterization of tin oxides by x-ray-photoemission spectroscopy, Phys. Rev. B **46**, 2460 (1992).

[38] K. K. D. Ehinon, S. Naille, R. Dedryvère, P.-E. Lippens, J.-C. Jumas, and D. Gonbeau, Ni_3Sn_4 electrodes for Li-ion batteries: Li-Sn alloying process and electrode/electrolyte interface phenomena, Chem. Mater. **20**, 5388 (2008).

[39] C. J. Powell and A. Jablonski, Consistency of calculated and measured electron inelastic mean free paths, J. Vac. Sci. Technol. A **17**, 1122 (1999).

[40] W. Tang, E. Sanville, and G. Henkelman, A grid-based Bader analysis algorithm without lattice bias, J. Phys.: Condens. Matter **21**, 084204 (2009).

[41] L. Köhler and G. Kresse, Density functional study of CO on Rh(111), Phys. Rev. B **70**, 165405 (2004).

[42] N. Pueyo Bellafont, F. Illas, and P. S. Bagus, Validation of Koopmans' theorem for density functional theory binding energies, Phys. Chem. Chem. Phys. **17**, 4015 (2015).

[43] V. Antonov, B. Harmon, and A. Yaresko, *Electronic Structure and Magneto-Optical Properties of Solids* (Springer, New York, 2004).

[44] M. J. van Setten, R. Costa, F. Viñes, and F. Illas, Assessing GW approaches for predicting core level binding energies, J. Chem. Theory Comput. **14**, 877 (2018).

[45] J. Nuss, C. Mühle, K. Hayama, V. Abdolazimi, and H. Takagi, Tilting structures in *inverse* perovskites, M_3TtO (M = Ca, Sr, Ba, Eu; Tt = Si, Ge, Sn, Pb), Acta Crystallogr. B **71**, 300 (2015).

[46] J. Thewlis and A. R. Davey, Thermal expansion of grey tin, Nature (London) **174**, 1011 (1954).

[47] N. Bouad, L. Chapon, R.-M. Marin-Ayral, F. Bouree-Vigneron, and J.-C. Tedenac, Neutron powder diffraction study of strain and crystallite size in mechanically alloyed PbTe, J. Solid State Chem. **173**, 189 (2003).